Three-Component Receptance Coupling Substructure Analysis for Tool Point Dynamics Prediction

Tony L. Schmitz[1]
e-mail: tschmitz@ufl.edu

G. Scott Duncan

Department of Mechanical and Aerospace Engineering,
University of Florida,
Gainesville, FL 32611

In this paper we present the second generation receptance coupling substructure analysis (RCSA) method, which is used to predict the tool point response for high-speed machining applications. This method divides the spindle-holder-tool assembly into three substructures: the spindle-holder base; the extended holder; and the tool. The tool and extended holder receptances are modeled, while the spindle-holder base subassembly receptances are measured using a "standard" test holder and finite difference calculations. To predict the tool point dynamics, RCSA is used to couple the three substructures. Experimental validation is provided. [DOI: 10.1115/1.2039102]

Keywords: high-speed machining, milling, stability, beam, finite element

1 Introduction

One area of manufacturing research that has made significant technological advancements in recent years is high-speed machining. Machine improvements include new spindle designs for higher rotational speed, torque, and power; increased slide speeds and accelerations; direct drive linear motor technology; and new machine designs for lower moving mass. The combination of new machine technology and tool material/coating developments often makes high-speed machining a viable alternative to other manufacturing processes. A key application example is the aerospace industry, where dramatic increases in material removal rates made possible using high-speed machining techniques have allowed designers to replace assembly-intensive sheet metal build-ups with monolithic aluminum components resulting in substantial cost savings [1].

A primary obstacle to the successful implementation of high-speed machining and full use of the available technology is chatter, or unstable machining. Many research efforts geared toward the understanding and avoidance of chatter have been carried out (e.g., see early studies in [2–11]). This work has led to the development of stability lobe diagrams that identify stable and unstable cutting zones as a function of the chip width and spindle speed. However, the methods used to produce these diagrams, whether analytic or time-domain, require knowledge of the tool point dynamics. The required dynamic model is typically obtained using impact testing, where an instrumented hammer is used to excite the tool at its free end (i.e., the tool point) and the resulting vibration is measured using an appropriate transducer, typically a low mass accelerometer. However, due to the large number of spindle, holder, and tool combinations, the required testing time can be significant. Therefore, a model which is able to predict the tool point response based on minimum input data is the preferred alternative.

The purpose of this paper is to build on the previous work of Schmitz et al. [12–15], which describes the tool point frequency response function, or receptance, prediction using the receptance coupling substructure analysis (RCSA) method. In these previous studies, a two component model of the machine-spindle-holder-tool assembly was defined. The machine-spindle-holder displacement-to-force receptance was recorded using impact testing, while the tool was modeled analytically. The tool and machine-spindle-holder substructure receptances were then coupled through translational and rotational springs and dampers; see the model in Fig. 1, where k_x and k_θ are the translational and rotational springs, c_x and c_θ are the translational and rotational viscous dampers, component A represents the tool, and component B the machine-spindle-holder. While the purpose of the springs and dampers between the tool and holder was to capture the effects of a potentially nonrigid, damped connection, it is likely that these connections also served to compensate for the fact that the displacement-to-moment, rotation-to-force, and rotation-to-moment receptances at the free end of the holder were assumed zero (i.e., perfectly rigid). Although it was shown in Ref. [15] that this two component model provides a valid approximation for a flexible tool clamped in a stiff spindle-holder, it does not offer the most generalized solution.

In order to enable RCSA predictions for a wider variety of machine-spindle-holder-tool combinations, an improved three-component model is presented here. In this model, the machine-spindle-holder substructure is separated into two parts: (1) the machine, spindle, holder taper, and portion of the holder nearest the spindle with standard geometry from one holder to another (hereafter referred to as the spindle-holder base subassembly); and (2) the remaining portion of the holder from the base to the free end (hereafter referred to as the extended holder subassembly). A technique for determining the rotation-to-force/moment and displacement-to-moment receptances for the free end of the spindle-holder base subassembly using only displacement-to-force measurements is also described. The experimental procedure involves direct and cross displacement-to-force measurements of a simple geometry "standard" holder clamped in the spindle to be modeled. The portion of the standard holder beyond the section with consistent geometry from holder-to-holder is then removed in simulation using an inverse receptance coupling approach (i.e., decomposition) to identify the four spindle-holder base subassembly receptances. These receptances are then coupled to models of the actual holder and tool. In the following sections, the method is described and experimental validation is presented.

---

[1] Author to whom correspondence should be addressed.

Contributed by the Manufacturing Engineering Division for publication in the ASME Journal of Manufacturing Science and Engineering. Manuscript received April 6, 2004; final revision received February 4, 2005. Review conducted by: Y. C. Shin.

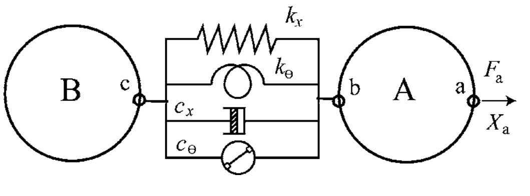

Fig. 1 Previous two-component RCSA model. An external force, $F_a(t)$, is applied to the free end of the tool (A) to determine the assembly X_a/F_a receptance. The tool is coupled to the machine-spindle-holder (B) through springs and dampers

2 Background and Notation

Substructure analysis, or component mode synthesis, methods have been used for several decades to predict the dynamic response of complicated assemblies using measurements and/or models of the individual components, or substructures. These components can be represented by spatial mass, stiffness, and damping data, modal data, or receptances (e.g., [16–30]). The latter representation is preferred in situations where the assembly receptances are the desired analysis output, as is the case in this research. For an assembly consisting of two rigidly connected substructures, as shown in Fig. 2, the assembly receptance, $G_{jk}(\omega)$, can be expressed as shown in Eq. (1), where ω is the frequency, X_j and Θ_j are the assembly displacement and rotation at coordinate j, and F_k and M_k are the force and moment applied to the assembly at coordinate k. If coordinate j is coincident with coordinate k, the receptance is referred to as a direct receptance; otherwise, it is a cross receptance. For the purposes of this paper, the nomenclature $G_{jk}(\omega)$ is used to describe the receptances that are produced when two substructures (or subassemblies) are coupled to produce the final assembly. The nomenclature $GS_{jk}(\omega)$ will replace $G_{jk}(\omega)$ in all relevant equations when two substructures (or subassemblies) are coupled that do not form the final assembly.

$$G_{jk}(\omega)=\begin{bmatrix}\frac{X_j}{F_k} & \frac{X_j}{M_k}\\ \frac{\Theta_j}{F_k} & \frac{\Theta_j}{M_k}\end{bmatrix}=\begin{bmatrix}H_{jk} & L_{jk}\\ N_{jk} & P_{jk}\end{bmatrix} \tag{1}$$

The substructure receptances, $R_{jk}(\omega)$, are defined in Eq. (2), where x_j and θ_j are the substructure displacement and rotation at coordinate j, and f_k and m_k are the force and moment applied to the substructure at coordinate k [15,31].

$$R_{jk}(\omega)=\begin{bmatrix}\frac{x_j}{f_k} & \frac{x_j}{m_k}\\ \frac{\theta_j}{f_k} & \frac{\theta_j}{m_k}\end{bmatrix}=\begin{bmatrix}h_{jk} & l_{jk}\\ n_{jk} & p_{jk}\end{bmatrix} \tag{2}$$

Based on the coordinates defined in Fig. 2, the equations to determine the assembly direct receptances, $G_{aa}(\omega)$ and $G_{dd}(\omega)$, and the assembly cross receptances, $G_{ad}(\omega)$ and $G_{da}(\omega)$, can be written as a function of the substructure receptances as shown in Eqs. (3)–(6), where rigid connections have been applied [32].

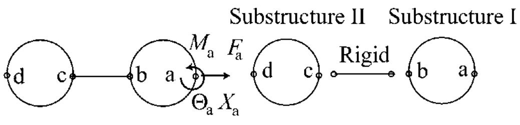

Fig. 2 Two-component assembly. The component responses are coupled through a rigid connection to give the assembly receptance(s)

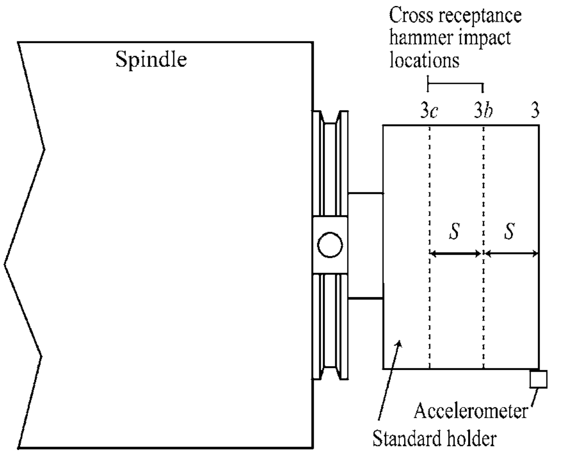

Fig. 3 Example standard holder for spindle-holder base subassembly receptance identification (dimensions provided in Table 1). Hammer impacts are completed at locations 3, 3*b*, and 3*c* to identify the required direct and cross receptances

$$G_{aa}(\omega)=\begin{bmatrix}\frac{X_a}{F_a} & \frac{X_a}{M_a}\\ \frac{\Theta_a}{F_a} & \frac{\Theta_a}{M_a}\end{bmatrix}=R_{aa}(\omega)-R_{ab}(\omega)[R_{bb}(\omega)+R_{cc}(\omega)]^{-1}R_{ba}(\omega) \tag{3}$$

$$G_{dd}(\omega)=\begin{bmatrix}\frac{X_d}{F_d} & \frac{X_d}{M_d}\\ \frac{\Theta_d}{F_d} & \frac{\Theta_d}{M_d}\end{bmatrix}=R_{dd}(\omega)-R_{dc}(\omega)[R_{bb}(\omega)+R_{cc}(\omega)]^{-1}R_{cd}(\omega) \tag{4}$$

$$G_{ad}(\omega)=\begin{bmatrix}\frac{X_a}{F_d} & \frac{X_a}{M_d}\\ \frac{\Theta_a}{F_d} & \frac{\Theta_a}{M_d}\end{bmatrix}=R_{ab}(\omega)[R_{bb}(\omega)+R_{cc}(\omega)]^{-1}R_{cd}(\omega) \tag{5}$$

$$G_{da}(\omega)=\begin{bmatrix}\frac{X_d}{F_a} & \frac{X_d}{M_a}\\ \frac{\Theta_d}{F_a} & \frac{\Theta_d}{M_a}\end{bmatrix}=R_{dc}(\omega)[R_{bb}(\omega)+R_{cc}(\omega)]^{-1}R_{ba}(\omega) \tag{6}$$

As noted, in order to populate the substructure receptance matrices, we apply measurement and modeling. Common modeling options include closed-form expressions for uniform Euler-Bernoulli beams [33] and finite element solutions (which can incorporate the more accurate Timoshenko beam model [34]). We consider both approaches in this study. As a convenience to the reader, the relevant analytical formulas and finite element Timoshenko stiffness and mass matrices are included in the Appendix.

3 Spindle-Holder Base Subassembly Identification

The experimental procedure used to determine the receptances at the free end of the spindle-holder base subassembly, $GS_{jk}(\omega)$, is described in this section. It is composed of three primary steps. First, the standard holder displacement-to-force direct and cross receptances are determined by impact testing. The standard holder geometry, which was selected to approximate a broad range of potential holders, is provided in Fig. 3. Second, these results are used to determine the three other direct receptances at the free end of the standard holder. Third, the section of the standard holder which is not common to other holders (see Fig. 4) is removed using inverse receptance coupling to determine all four spindle-holder base subassembly receptances. Each step of the procedure is described in the following sections. Example results are included.

3.1 Standard Test Holder Receptances Once the standard holder is mounted in a spindle (see Fig. 3), the four subassembly

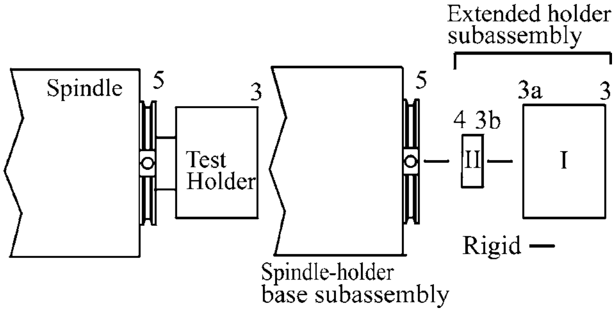

Fig. 4 Standard holder substructures for inverse receptance coupling

receptances are determined by measuring the direct, H_{33}, and cross, H_{33b}, and H_{33c}, displacement-to-force receptances on the standard holder, applying a second-order backward finite difference method to find L_{33} (and, equivalently, N_{33}) [35], and then synthesizing P_{33}. For the cross displacement-to-force measurements, the distance S should be selected to increase the difference in relative amplitudes between H_{33}, H_{33b}, and H_{33c} without leading to a poor signal-to-noise ratio for the H_{33c} measurement (i.e., many of the lower frequency spindle-holder modes resemble a fixed-free fundamental mode shape and have very small amplitudes near the spindle face for the bandwidth of interest). Practically, we have observed that the finite difference results improve as S is increased; however, care must be taken to ensure that the location of the H_{33c} measurement provides sufficient signal-to-noise. The receptance L_{33} is determined from the measured displacement-to-force receptances using Eq. (7). By reciprocity, N_{33} can be set equal to L_{33}. The remaining receptance, P_{33}, is synthesized from H_{33}, L_{33}, and N_{33}, as shown in Eq. (8) [27].

$$L_{33} = \frac{3H_{33} - 4H_{33b} + H_{33c}}{2S} \tag{7}$$

$$P_{33} = \frac{\Theta_3}{M_3} = \frac{F_3}{X_3}\frac{X_3}{M_3}\frac{\Theta_3}{F_3} = \frac{1}{H_{33}}L_{33}N_{33} = \frac{L_{33}{}^2}{H_{33}} \tag{8}$$

Due to the subtraction of the similarly scaled H_{33}, H_{33b}, and H_{33c} receptances, noise in the measurement data can detrimentally affect the quality of L_{33} and N_{33} (produced by the finite-difference method) and, therefore, P_{33}. To reduce the noise effect, the measured receptance data were smoothed using a Savitzky-Golay filter, which performs a local polynomial regression to determine the smoothed value for each data point [36], prior to the application of Eq. (7). For this study, filters with polynomial orders of two or three were applied over windows of 31 to 81 data points.

3.2 Extended Holder Subassembly Model. The extended holder subassembly for the steel standard holder consisted of solid, cylindrical substructures I and II as shown in Fig. 4. Equations (9)–(12) provide the direct and cross extended holder subassembly receptance matrices, where rigid coupling has been applied. These equations were determined from Eqs. (3)–(6) by appropriate substitutions.

$$GS_{33}(\omega) = \begin{bmatrix} \frac{X_3}{F_3} & \frac{X_3}{M_3} \\ \frac{\Theta_3}{F_3} & \frac{\Theta_3}{M_3} \end{bmatrix} = R_{33}(\omega) - R_{33a}(\omega)[R_{3a3a}(\omega) + R_{3b3b}(\omega)]^{-1}R_{3a3}(\omega) \tag{9}$$

$$GS_{44}(\omega) = \begin{bmatrix} \frac{X_4}{F_4} & \frac{X_4}{M_4} \\ \frac{\Theta_4}{F_4} & \frac{\Theta_4}{M_4} \end{bmatrix} = R_{44}(\omega) - R_{43b}(\omega)[R_{3b3b}(\omega) + R_{3a3a}(\omega)]^{-1}R_{3b4}(\omega) \tag{10}$$

Table 1 Standard holder substructure parameters

	I	II
Coordinate j	3	3b
Coordinate k	3a	4
d_o (mm)	63.3	52.7
L (mm)	62.8	16.3
ρ (kg/m^3)	7800	
E (N/m^2)	2×10^{11}	
η	0.0015	

$$GS_{34}(\omega) = \begin{bmatrix} \frac{X_3}{F_4} & \frac{X_3}{M_4} \\ \frac{\Theta_3}{F_4} & \frac{\Theta_3}{M_4} \end{bmatrix} = R_{33a}(\omega)[R_{3a3a}(\omega) + R_{3b3b}(\omega)]^{-1}R_{3b4}(\omega) \tag{11}$$

$$GS_{43}(\omega) = \begin{bmatrix} \frac{X_4}{F_3} & \frac{X_4}{M_3} \\ \frac{\Theta_4}{F_3} & \frac{\Theta_4}{M_3} \end{bmatrix} = R_{43b}(\omega)[R_{3a3a}(\omega) + R_{3b3b}(\omega)]^{-1}R_{3a3}(\omega) \tag{12}$$

3.3 Spindle-Holder Base Subassembly Receptance. The spindle-holder base subassembly receptance matrix, $G_{33}(\omega)$, can be expressed as shown in Eq. (13) by rewriting Eq. (3). The left-hand side of this equation is known once the steps described in Sec. 3.1 are completed. Also, the extended holder subassembly receptances, GS_{33}, GS_{44}, GS_{34}, and GS_{43}, are determined using the equations provided in Sec. 3.2. Therefore, Eq. (13) can be rewritten to solve for the spindle-holder base subassembly receptances, $GS_{55}(\omega)$. See Eq. (14).

$$G_{33}(\omega) = \begin{bmatrix} H_{33} & L_{33} \\ N_{33} & P_{33} \end{bmatrix} = GS_{33}(\omega) - GS_{34}(\omega)[GS_{44}(\omega) + GS_{55}(\omega)]^{-1}GS_{43}(\omega) \tag{13}$$

$$GS_{55}(\omega) = \begin{bmatrix} \frac{x_5}{f_5} & \frac{x_5}{m_5} \\ \frac{\theta_5}{f_5} & \frac{\theta_5}{m_5} \end{bmatrix} = GS_{34}(\omega)[GS_{33}(\omega) - G_{33}(\omega)]^{-1} \times GS_{43}(\omega) - GS_{44}(\omega) \tag{14}$$

Tests were completed to determine $GS_{55}(\omega)$ for a 24,000 rpm/40 kW direct drive spindle (HSK 63A interface) using a steel standard holder. The dimensions and material properties for the standard holder substructures are provided in Table 1, where d_o is the diameter, L is the length, ρ is the density, and η is the frequency-independent damping coefficient. The η values used in this study were determined experimentally from free-free testing of representative cylindrical rods. During the measurement of the direct and cross receptances for the mounted standard holder, the distance S was selected as 25.40 mm. The resulting spindle receptances, h_{55}, l_{55}, and p_{55}, are shown in Fig. 5. These results are based on the average of 15 complete measurement sets (H_{33}, H_{33b}, and H_{33c}—each the average of ten impacts). Our experience has shown that averaging is the most effective technique for reducing the inherent noise amplification during the finite difference computations.

As shown in Eq. (14), the Fig. 5 result was determined by removing the extended holder subassembly for the standard holder from the complete assembly in simulation. Because the measurement bandwidth for high-speed/high-power spindle testing is typically 5 kHz or less, we have found that it makes no practical difference whether the Euler-Bernoulli or Timoshenko beam model is used to describe the standard holder substructure(s). The standard holder behaves basically as an inertial mass since its

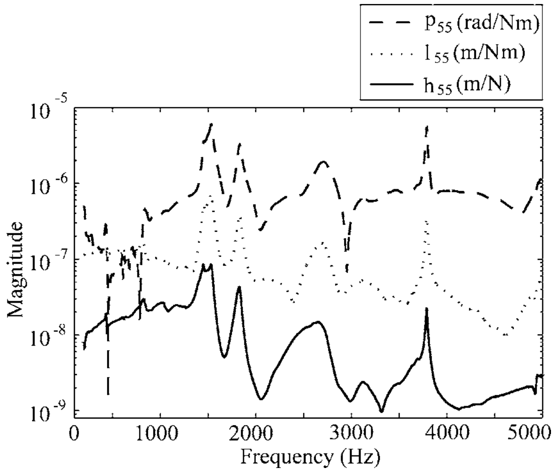

Fig. 5 Spindle receptances $G_{55}(\omega)$ determined from standard holder direct and cross receptance measurements

clamped-free bending mode fundamental natural frequency, for the geometry used in this study, is outside the bandwidth of interest.

3.4 Holder Experimental Verification. Once the 24,000 rpm/40 kW spindle-holder base subassembly receptances, $GS_{55}(\omega)$, were determined, it was possible to couple this result to arbitrary holder geometries to predict the receptance at any coordinate on the machine-spindle-holder assembly. To validate the procedure, a tapered thermal shrink fit holder (25.3 mm bore) with an HSK 63A spindle interface was divided into 12 substructures beyond the spindle-holder base subassembly as shown in Fig. 6. Each substructure was assumed to be a hollow or solid cylindrical steel beam, as appropriate. Table 2 provides the holder geometry and assumed material properties.

The first step in predicting the assembly response, as described in Sec. 3.2, was to couple substructures I–XII to produce the direct and cross extended holder subassembly receptances at coordinates 3 and 4. With the increase in substructures from 2 to 12, the Sec. 3.2 procedure remained the same; however, substructure I was first coupled to substructure II, then the resulting subassembly was coupled to substructure III, and so on to produce the required extended holder subassembly receptances.

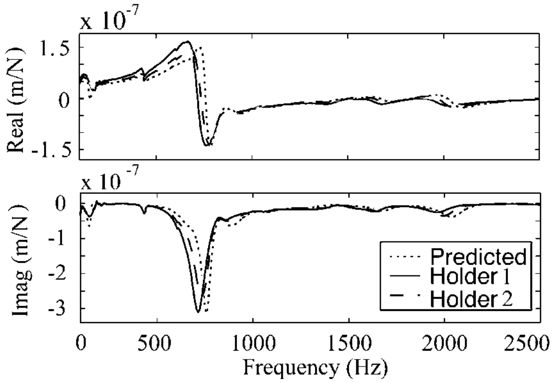

Fig. 7 Measured (two nominally identical holders) and predicted H_{33} results for tapered thermal shrink fit holder (25.3 mm bore)

The next step was to rigidly couple the spindle-holder base subassembly (determined in the previous section and shown in Fig. 5) to the extended holder subassembly using Eq. (13) to determine the receptances at the free end of the holder, $G_{33}(\omega)$. Figure 7 shows the predicted H_{33} result as well as measurements for two nominally identical holders. The Euler-Bernoulli beam model was applied to develop the extended holder receptances in this case.

4 Tool Point Response Prediction

To predict the tool point dynamics, the modeling procedure was again applied to the 24,000 rpm/40 kW spindle (HSK 63A interface) using a tapered thermal shrink holder with a 19.1 mm carbide tool blank inserted as shown in Fig. 8. The assembly was divided into the spindle-holder base subassembly and 13 cylindrical substructures of differing diameters; see Table 3. To model the receptances, a composite modulus and mass were substituted for substructures II–VIII to account for the material differences between the steel holder and the carbide tool blank. Also, the mass expression for these substructures (provided in the Appendix) was replaced with the composite mass shown in Eq. (15), where ρ_h and ρ_t are the density of the holder and tool, respectively. Additionally, the product of the elastic modulus and second area moment of inertia, EI, was replaced by the product shown in Eq. (16), where E_h is the holder modulus, E_t is the tool material modulus, and I_h and I_t are the second area moments of inertia for the holder and tool, respectively. The substructure parameters are shown in Table 3.

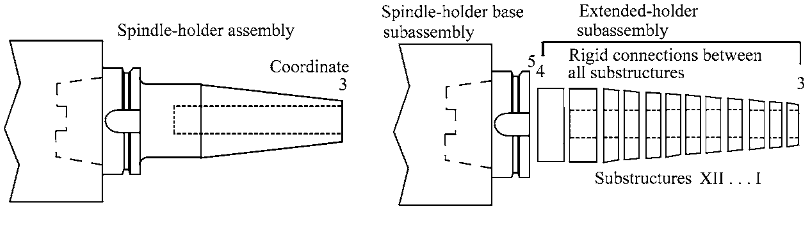

Fig. 6 Tapered thermal shrink fit holder (25.3 mm bore) substructure model

Table 2 Tapered thermal shrink fit holder (25.3 mm bore) substructure parameters

Substructure	I	II	III	IV	V	VI	VII	VIII	IX	X	XI	XII
d_i (mm)	25.3	25.3	25.3	25.3	25.3	25.3	25.3	26.0	26.0	26.0	26.0	-
d_o (mm)	44.2	45.1	46.1	47.0	47.9	48.9	49.8	50.7	51.7	52.6	52.6	52.6
L (mm)	5.5	5.5	5.5	5.5	5.5	5.5	5.5	5.5	5.5	5.5	15.7	30.3
ρ (kg/m^3)						7800						
E (N/m^2)						2×10^{11}						
η						0.0015						

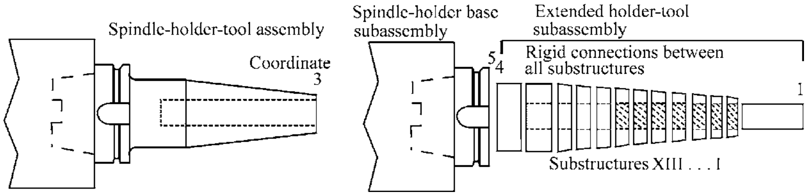

Fig. 8 Tapered thermal shrink fit holder with 19.1-mm-diam tool blank substructure model

$$m = \frac{\pi(\rho_h(d_o^2 - d_i^2) + \rho_t d_i^2)L}{4} \tag{15}$$

$$EI = E_hI_h + E_tI_t = \frac{E_h\pi(d_o^4 - d_i^4) + E_t\pi d_i^4}{64} \tag{16}$$

The next step was to rigidly couple substructures I through XIII to produce the direct and cross extended holder-tool subassembly receptances at coordinates 1 and 4. The final step in the procedure was to predict the tool point dynamics by rigidly coupling the extended holder-tool subassembly to the spindle-holder base subassembly. With the appropriate coordinate substitution in Eq. (13), the tool point receptance, $G_{11}(\omega)$, was determined according to Eq. (17), where the receptances associated with coordinates 1 and 4 are the extended holder-tool subassembly direct and cross receptances. The predicted and measured assembly tool point displacement-to-force receptances, H_{11}, are displayed in Fig. 9. In this figure, results for both Euler-Bernoulli and Timoshenko (finite element) beam models are provided. It is seen that the finite element model (100 elements were used for each substructure) dominant natural frequency is closer to the measured result, as expected. However, the predicted natural frequency is still approximately 50 Hz higher. This disagreement is explored in Sec. 5.3.

$$G_{11}(\omega) = \begin{bmatrix} H_{11} & L_{11} \\ N_{11} & P_{11} \end{bmatrix} = GS_{11}(\omega) - GS_{14}(\omega)[GS_{44}(\omega) + GS_{55}(\omega)]^{-1}GS_{41}(\omega) \tag{17}$$

5 Case Studies

5.1 Geared Quill-Type Spindle. In this section, prediction and measurement results are provided for two cutters coupled to a geared, quill-type spindle with a CAT-50 spindle-holder interface (Big-Plus tool holders were used which include both taper and face contact). The spindle-holder base subassembly receptances were determined using a steel cylindrical standard holder (63.4 mm diameter and 89.0 mm length); the cross FRF measurements were again recorded at distances of 25.4 mm and 50.8 mm from the free end of the standard holder. The substructure receptances for the solid body tools (i.e., both cutting tools were composed of solid steel modular bodies with carbide inserts attached) were then computed and the tool point FRF predicted by rigidly coupling the tool models to the spindle measurements.

Figure 10 displays the H_{11} results for an inserted endmill with 4 “flutes” (20 total inserts). The tool body geometry is defined in Table 4 (as before substructure I is nearest the free end of the clamped cutter). Figure 11 shows the H_{11} measurement and prediction for a 28-insert facemill (see Table 5). In both cases, Euler-Bernoulli beam models were employed to describe the standard holder and cutter bodies.

5.2 Geared Spindle Comparison. In this section, the spindle-holder base subassembly receptances were measured on two nominally identical, geared spindles (CAT-50 holder-spindle interface). The steel cylindrical standard holder was 63.4 mm in diameter and 89.0 mm long. The cross FRF measurement locations were the same as specified previously. Figure 12 provides standard holder direct FRF measurement results for both spindles. Three curves are shown: the solid line (line 1a) represents the average of five measurement sets (10 impacts each) completed without removing the holder from the first spindle (i.e., spindle 1); the dotted line gives the average of three more spindle 1 measurements after removing and replacing the holder (line 1b); and the dashed line shows the average of five spindle 2 measurements (line 2). These curves show that, although the spindles are similar, the difference between the spindle dynamics is larger than the measurement divergence.

Next, a 16-insert solid body facemill was inserted in spindle 1 and the tool point FRF recorded. Predictions were finally completed using both the spindle 1 and 2 receptances. This result is provided in Fig. 13; the facemill geometry and material properties are given in Table 6. It is seen that the prediction completed using the spindle 1 receptances (dashed line) more accurately identifies the spindle 1 measured frequency content (solid line). Therefore, it would be necessary to measure both spindles to make accurate predictions, rather than relying on manufacturing repeatability. It has been our experience that the dynamic consistency between spindles is manufacturer-dependent.

5.3 Shrink Fit Holder With Varying Tool Length. In this study 30 carbide tool blanks were sequentially inserted in a tapered thermal shrink fit holder and the tool point response recorded. The insertion length was maintained at 22.9 mm while the overhang length varied from 66.0 to 142.2 mm in increments of 2.5 mm (the 139.7 overhang length test was not completed) for the 19.1-mm-diam tool blanks. These measurements were completed on a 16,000 rpm direct drive spindle with an HSK 63A spindle-holder interface. The substructure information is provided in Table 7. The 30 measurement results are shown in the top panel of Fig. 14, while the bottom panel shows the h_{55} spindle response

Table 3 Tapered thermal shrink fit holder and 19.1 mm diameter tool blank substructure parameters

Substructure	I	II	III	IV	V	VI	VII	VIII	IX	X	XI	XII	XIII
d_i (mm)	-	19.1	19.1	19.1	19.1	19.1	19.1	19.1	19.1	19.1	19.1	19.1	-
d_o (mm)	19.1	33.4	34.4	35.4	36.4	37.5	38.5	39.5	39.5	40.4	41.4	41.4	41.4
L (mm)	111.9	5.8	5.8	5.8	5.8	5.8	5.8	5.8	4.1	4.1	4.1	10.6	37.4
ρ (kg/m^3)	7800 (steel holder) 14,500 (carbide tool blank)												
E (N/m^2)	2×10^{11} (steel holder) 5.85×10^{11} (carbide tool blank)												
η	0.0015												

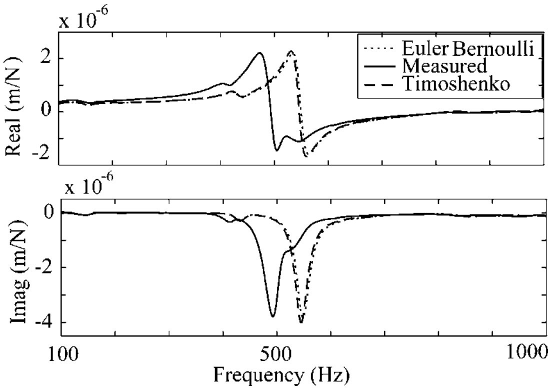

Fig. 9 Measured and predicted H_{11} results for tapered thermal shrink fit holder with 19.1-mm-diam tool blank (111.9 mm overhang length)

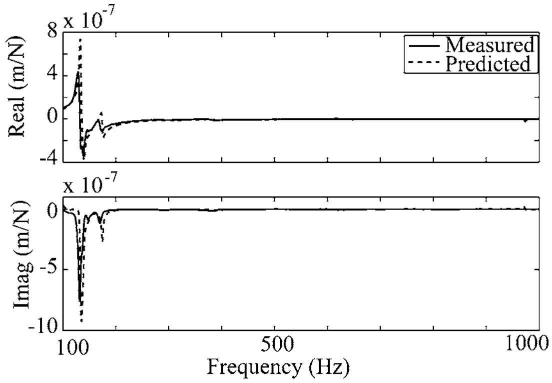

Fig. 11 Measured and predicted H_{11} results for 28-insert facemill

(i.e., after removing the extended portion of the standard holder in simulation). It is seen in the top panel that, although the general trend is increased amplitude and reduced frequency with increasing overhang length, the tool point magnitudes are attenuated near 800 and 1200 Hz. This is due to dynamic interaction between the tool clamped-free mode and the spindle modes [37]. The fact that the spindle natural frequencies agree with the locations of the dynamic interactions (see bottom panel of Fig. 14) suggests that the spindle response has been properly identified.

Predictions of the tool point responses using the spindle receptances and Timoshenko beam elements (100 for each substructure) to model the tool and holder showed similar disagreement in natural frequency to the results provided in Fig. 9. Reasonable perturbations to the model parameters were unable to close the approximately 50 Hz gap. Therefore, translational and rotational springs and viscous dampers (as shown in Fig. 1) were inserted between the holder and tool to account for what was presumed to be a nonrigid connection (even for the shrink fit test case studied here). The spring and damper values were then determined using a nonlinear least-squares best fit [15]. The least-squares algorithm was initiated using connection parameters obtained from a visual fit and continued until the frequency-dependent residual between the predicted and measured H_{11} results was less than 1×10^{-15} m/N. The four parameter values were constrained to be zero or greater, but no other restrictions were applied. The average values for the connection parameters (see Table 8) were then used to make predictions for various overhang lengths. The predictions were carried out using Eq. (18), where

$$K = \begin{bmatrix} k_x + i\omega c_x & 0 \\ 0 & k_\theta + i\omega c_\theta \end{bmatrix}.$$

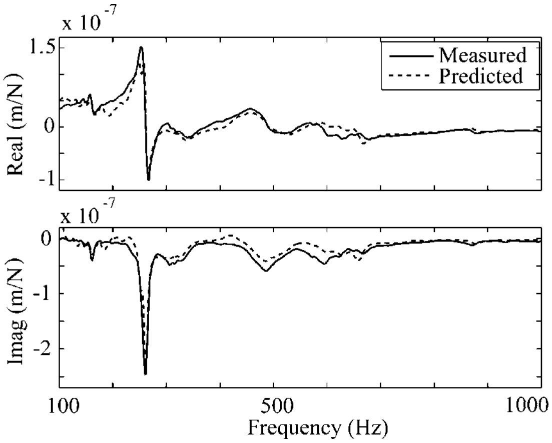

Fig. 10 Measured and predicted H_{11} results for 20-insert endmill

Table 4 Solid body endmill (20 inserts) substructure parameters

Substructure	I	II	III
d_o (mm)	99.8	80.1	69.9
L (mm)	85.6	94.9	16.8
ρ (kg/m^3)		7800	
E (N/m^2)		2×10^{11}	
η		0.0015	

Table 5 Solid body facemill (28 inserts) substructure parameters

Substructure	I	II	III	IV
d_o (mm)	126.2	130.3	80.0	69.9
L (mm)	55.0	18.3	62.7	18.3
ρ (kg/m^3)		7800		
E (N/m^2)		2×10^{11}		
η		0.0015		

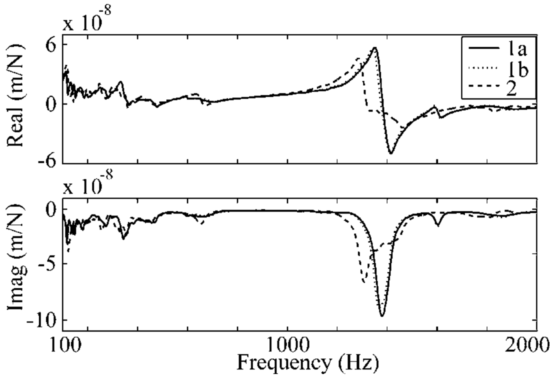

Fig. 12 Standard holder direct receptances for two nominally identical, geared spindles (CAT-50 holder-spindle interface). Line 1a (solid) shows the average of five measurement sets completed without removing the holder from spindle 1; line 1b (dotted) gives the average of three more spindle 1 measurements after removing and replacing the holder; line 2 (dashed) shows the average of five spindle 2 measurements

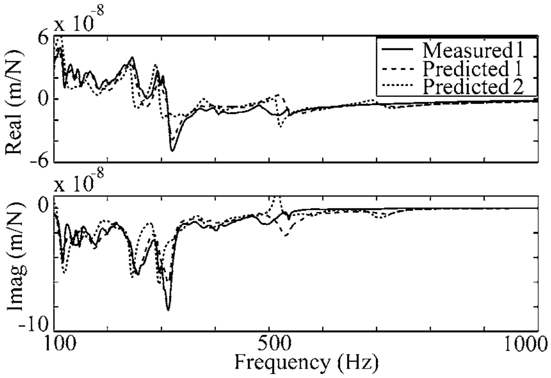

Fig. 13 Measured and predicted H_{11} results for 16-insert facemill. Results are shown for predictions from spindle 1 (dashed) and spindle 2 (dotted) standard holder measurements. Measurement recorded using spindle 1

$$G_{11}(\omega) = \begin{bmatrix} H_{11} & L_{11} \\ N_{11} & P_{11} \end{bmatrix} = GS_{11}(\omega) - GS_{14}(\omega)[GS_{44}(\omega) + GS_{55}(\omega) + K^{-1}]GS_{41}(\omega) \qquad (18)$$

Figure 15 shows the measured and predicted results for four different overhang lengths. These lengths were selected to provide results: (1) near the 1200 Hz interaction frequency shown in Fig. 14 (76.2 mm); (2) between the interactions at 800 and 1200 Hz (94.0 mm); (3) near the 800 Hz interaction (106.7 mm); and (4) to the left of the 800 Hz interaction (132.1 mm). Reasonable agreement is observed in all cases. To determine the impact of the residual disagreement, however, stability lobes were constructed using the 94.0 mm overhang case for both the measured and predicted tool point receptances [38]. A 50% radial immersion upmilling cut using a four-flute cutter with cutting force coefficients of 800 N/mm^2 and 0.3 was assumed for demonstration purposes. This result is provided in Fig. 16. Although there is a shift toward lower speeds for the lobes computed using the predicted receptance (due to the underprediction of the natural frequency), the diagram does not exhibit extreme sensitivity to this frequency error. Based on this result, while the use of finite connection stiffness values, i.e., a nonzero K^{-1} matrix in Eq. (18), may improve the receptance prediction accuracy, a rigid connection appears to be adequate to guide the selection of stable cutting conditions provided points near the stability boundaries are not chosen.

Table 6 Solid body facemill (16 inserts) substructure parameters

Substructure	I	II	III
d_o (mm)	279.4	63.5	69.9
L (mm)	27.2	88.9	15.9
ρ (kg/m^3)		7800	
E (N/m^2)		2×10^{11}	
η		0.0015	

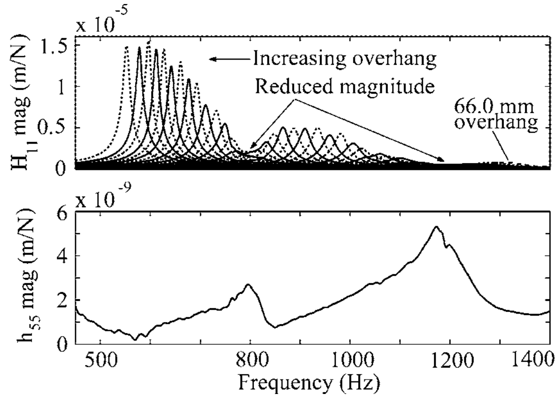

Fig. 14 Measurement results for thermal shrink fit tool holder-tool blank case study. (Top panel) 30 different carbide blanks were sequentially inserted and the tool point receptance recorded. (Bottom panel) The spindle displacement-to-force receptance identified using the standard holder

6 Conclusions

Tool point dynamics prediction using the second generation RCSA method was demonstrated. The improved method includes the following features: (1) separation of the spindle-holder-tool assembly into three substructures—the spindle-holder base, extended holder, and tool; (2) experimental identification of the spindle-holder base subassembly translational and rotational receptances using a finite difference approach; (3) analytical and finite element modeling of the holder and tool substructure receptances; and (4) rigid coupling of the spindle-holder base subassembly to the extended holder and rigid or flexible/damped coupling of the tool to this result to determine the tool point response. Experimental validation of the method was provided for multiple spindle-holder-tool setups.

Acknowledgments

This work was partially supported by the National Science Foundation (Grant No. DMI-0238019), the Office of Naval Research (2003 Young Investigator Program), the Naval Surface Warfare Center—Carderock Division, and BWXT Y-12. Any opinions, findings, and conclusions or recommendations expressed in this material are those of the authors and do not necessarily reflect the views of these agencies. The authors also wish to acknowledge contributions to the development of the RCSA method by Dr. M. Davies, University of North Carolina-Charlotte, Charlotte, NC, and Dr. T. Burns, National Institute of Standards and Technology, Gaithersburg, MD. They also acknowledge Mr. R. Ketron, Caterpillar, Inc., Aurora, IL, Ms. J. Dyer, Eastside High School, Gainesville, FL, Mr. Duke Hughes, BWXT Y-12, Oak Ridge, TN, and Dr. P. Jacobs, BWXT Y-12, for their assistance in collecting portions of the data used in this study.

Table 7 Shrink fit holder case study substructure parameters

Substructure	I	II	III	IV	V	VI
d_i (mm)	-	19.1	19.1	19.1	21	6
d_o (mm)	19.1	35.0	36.1	37.3	38.2	38.5
L (mm)	Varied	11.4	11.4	9.1	25.0	17.0
ρ (kg/m^3)	7800 (steel holder) 14,500 (carbide tool blank)					
E (N/m^2)	2×10^{11} (steel holder) 5.85×10^{11} (carbide tool blank)					
η	0.0015					

Table 8 Connection parameters for shrink fit holder case study

k_x(N/m)	k_θ(N/rad)	c_x(N s/m)	c_θ(N s/rad)
6.5×10^7	3.4×10^6	520	3540

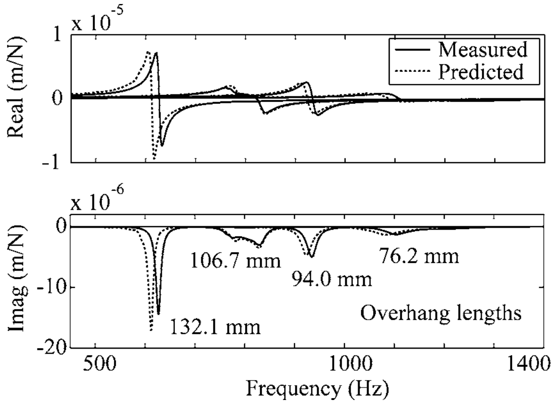

Fig. 15 Measured and predicted H_{11} results for four different overhang lengths (132.1, 106.7, 94.0, and 76.2 mm). The overhang length for each of the four results is identified. Predictions were completed using the flexible/damped connection (connection parameters are provided in Table 8)

Appendix: Beam Receptance Modeling

Bishop and Johnson [33] showed that the displacement and rotation-to-force and moment receptances for uniform Euler-Bernoulli beams could be represented by simple closed-form expressions. For a cylindrical free-free beam with coordinates j and k identified at each end, the frequency-dependent direct and cross receptances are given by:

$$h_{jj}=h_{kk}=\frac{-F_5}{EI(1+i\eta)\lambda^3F_3}\quad h_{jk}=h_{kj}=\frac{F_8}{EI(1+i\eta)\lambda^3F_3}\tag{A1}$$

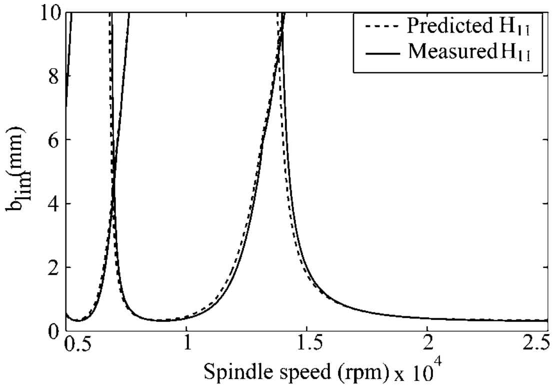

Fig. 16 Example stability lobes (50% radial immersion up-milling cut using a four-flute cutter with cutting force coefficients of 800 N/mm² and 0.3) developed using measured (solid line) and predicted (dotted line) H_{11} results for 94.0 mm overhang length

$$l_{jj}=-l_{kk}=\frac{-F_1}{EI(1+i\eta)\lambda^2F_3}\quad l_{jk}=-l_{kj}=\frac{F_{10}}{EI(1+i\eta)\lambda^2F_3}\tag{A2}$$

$$n_{jj}=-n_{kk}=\frac{-F_1}{EI(1+i\eta)\lambda^2F_3}\quad n_{jk}=-n_{kj}=\frac{-F_{10}}{EI(1+i\eta)\lambda^2F_3}\tag{A3}$$

$$p_{jj}=p_{kk}=\frac{F_6}{EI(1+i\eta)\lambda F_3}\quad p_{jk}=p_{kj}=\frac{F_7}{EI(1+i\eta)\lambda F_3}\tag{A4}$$

where E is the elastic modulus, I is the second area moment of inertia, η is the frequency-independent damping coefficient (damping was not included in Bishop and Johnson, but has been added as part of this analysis), and:

$$\lambda^4=\frac{\omega^2m}{EI(1+i\eta)L}\tag{A5}$$

$$\begin{gathered}F_1=\sin\lambda L\sinh\lambda L\quad F_3=\cos\lambda L\cosh\lambda L-1\quad F_5=\cos\lambda L\sinh\lambda L-\sin\lambda L\cosh\lambda L\\ F_6=\cos\lambda L\sinh\lambda L+\sin\lambda L\cosh\lambda L\qquad F_7=\sin\lambda L+\sinh\lambda L\\ F_8=\sin\lambda L-\sinh\lambda L\qquad F_{10}=\cos\lambda L-\cosh\lambda L.\end{gathered}\tag{A6}$$

In Eq. (A5), the cylindrical beam mass is given by

$$m=\frac{\pi(d_o^2-d_i^2)L\rho}{4},$$

where d_o is the outer diameter, d_i is the inner diameter (set equal to zero if the beam is not hollow), L is the length, and ρ is the density; the cylinder's second area moment of inertia is

$$I=\frac{\pi(d_o^4-d_i^4)}{64};$$

and ω is the frequency (in rad/s).

The Timoshenko beam model, which includes the effects of rotary inertia and shear, was implemented using finite elements [34]. Each four degree-of-freedom (rotation and displacement at both ends) free-free beam section was modeled using appropriate mass, M, and stiffness, K, matrices [39]. The mass matrix was:

$$M = \frac{\rho A l}{(1+\phi)^2}\begin{bmatrix} \frac{13}{35}+\frac{7\phi}{10}+\frac{\phi^2}{3} & \left(\frac{11}{210}+\frac{11\phi}{120}+\frac{\phi^2}{24}\right)l & \frac{9}{70}+\frac{3\phi}{10}+\frac{\phi^2}{6} & -\left(\frac{13}{420}+\frac{3\phi}{40}+\frac{\phi^2}{24}\right)l \\ & \left(\frac{1}{105}+\frac{\phi}{60}+\frac{\phi^2}{120}\right)l^2 & \left(\frac{13}{420}+\frac{3\phi}{40}+\frac{\phi^2}{24}\right)l & -\left(\frac{1}{140}+\frac{\phi}{60}+\frac{\phi^2}{120}\right)l^2 \\ & & \frac{13}{35}+\frac{7\phi}{10}+\frac{\phi^2}{3} & -\left(\frac{11}{210}+\frac{11\phi}{120}+\frac{\phi^2}{24}\right)l \\ \text{Symmetric} & & & \left(\frac{1}{105}+\frac{\phi}{60}+\frac{\phi^2}{120}\right)l^2 \end{bmatrix}$$

$$+ \frac{\rho A l}{(1+\phi)^2}\left(\frac{r_g}{l}\right)^2\begin{bmatrix} \frac{6}{5} & \left(\frac{1}{10}-\frac{\phi}{2}\right)l & -\frac{6}{5} & \left(\frac{1}{10}-\frac{\phi}{2}\right)l \\ & \left(\frac{2}{15}+\frac{\phi}{6}+\frac{\phi^2}{3}\right)l^2 & -\left(\frac{1}{10}-\frac{\phi}{2}\right)l & -\left(\frac{1}{30}+\frac{\phi}{6}+\frac{\phi^2}{6}\right)l^2 \\ & & \frac{6}{5} & -\left(\frac{1}{10}-\frac{\phi}{2}\right)l \\ \text{Symmetric} & & & \left(\frac{2}{15}+\frac{\phi}{6}+\frac{\phi^2}{3}\right)l^2 \end{bmatrix}$$

where A is the cross-sectional area, l is the section length, r_g is the radius of gyration, and ϕ is a shear deformation parameter given by

$$\phi = \frac{12EI(1+\eta)}{k'GAl^2},$$

where

$$G = \frac{E}{2(1+\nu)}$$

is the shear modulus (ν is Poisson's ratio) and k' is the shear coefficient which depends on the cross-section shape and ν [40]. The stiffness matrix (which included damping) was:

$$K = \frac{EI(1+i\eta)}{l^3(1+\phi)^2}\begin{bmatrix} 12 & 6l & -12 & 6l \\ & (4+2\phi+\phi^2)l^2 & -6l & (2-2\phi-\phi^2)l^2 \\ & & 12 & -6l \\ \text{Symmetric} & & & (4+2\phi+\phi^2)l^2 \end{bmatrix}$$

$$+ \frac{k'AG\phi^2}{4l(1+\phi)^2}\begin{bmatrix} 4 & 2l & -4 & 2l \\ & l^2 & -2l & l^2 \\ & & 4 & -2l \\ \text{Symmetric} & & & l^2 \end{bmatrix}$$

The element M and K matrices were then collected into the global mass, $\boldsymbol{M}$, and stiffness, $\boldsymbol{K}$, matrices using Guyan reduction [34] and the resulting equation of motion solved in the frequency domain. See Eq. (A7), where n elements have been applied.

$$[-\boldsymbol{M}\omega^2+\boldsymbol{K}]\cdot\begin{bmatrix} x_1 \\ \theta_1 \\ x_2 \\ \theta_2 \\ \vdots \\ x_{n+1} \\ \theta_{n+1} \end{bmatrix} = \begin{bmatrix} f_1 \\ m_1 \\ f_2 \\ m_2 \\ \vdots \\ f_{n+1} \\ m_{n+1} \end{bmatrix} \tag{A7}$$

References

[1] Halley, J., Helvey, A., Smith, K. S., and Winfough, W. R., 1999, "The Impact of High-Speed Machining on the Design and Fabrication of Aircraft Components," *Proc. of the 17th Biennial Conference on Mechanical Vibration and Noise, ASME Design and Technical Conferences*, Las Vegas, NV, September 12–16.

[2] Arnold, R. N., 1946, "The Mechanism of Tool Vibration in the Cutting of Steel," Proc. Inst. Mech. Eng., **154**, pp. 261–284.

[3] Tobias, S. A., and Fishwick, W., 1958, "The Chatter of Lathe Tools under Orthogonal Cutting Conditions," Trans. ASME, **80**, p. 1079.

[4] Tlusty, J., and Polocek, M., 1963, "The Stability of the Machine-Tool Against Self-Excited Vibration in Machining," *Proc. of the International Research in Production Engineering Conference*, Pittsburgh, PA, ASME, NY, p. 465.

[5] Tobias, S. A., 1965, *Machine-Tool Vibration*, Blackie and Sons Ltd., Glasgow, Scotland.

[6] Koenisberger, F., and Tlusty, J., 1967, *Machine Tool Structures—Vol. I: Stability Against Chatter*, Pergamon, NY

[7] Merrit, H., 1965, "Theory of Self-Excited Machine Tool Chatter," J. Eng. Ind., **87**, pp. 447–454.

[8] Kegg, R. L., 1965, "Cutting Dynamics in Machine Tool Chatter," J. Eng. Ind., **87**, pp. 464–470.

[9] Shridar, R., Hohn, R. E., and Long, G. W., 1968, "A General Formulation of the Milling Process Equation," J. Eng. Ind., **90**, p. 317.

[10] Shridar, R., Hohn, R. E., and Long, G. W., 1968, "A Stability Algorithm for the General Milling Process," J. Eng. Ind., **90**, p. 330.

[11] Hanna, N. H., and Tobias, S. A., 1974, "A Theory of Nonlinear Regenerative Chatter," J. Eng. Ind., **96**, pp. 247–255.

[12] Schmitz, T., and Donaldson, R. 2000, "Predicting High-Speed Machining Dynamics by Substructure Analysis," CIRP Ann., **49**, pp. 303–308.

[13] Schmitz, T., Davies, M., and Kennedy, M., 2001, "Tool Point Frequency Response Prediction for High-Speed Machining by RCSA," J. Manuf. Sci. Eng., **123**, pp. 700–707.

[14] Schmitz, T., Davies, M., Medicus, K., and Snyder, J., 2001, "Improving High-Speed Machining Material Removal Rates by Rapid Dynamic Analysis," CIRP Ann., **50**, pp. 263–268.

[15] Schmitz, T., and Burns, T., 2003, "Receptance Coupling for High-Speed Machining Dynamics Prediction," *Proc. of the 21st International Modal Analysis Conference*, February 3–6, Kissimmee, FL (on CD).

[16] Bishop, R. E. D., and Johnson, D. C., 1960, *The Mechanics of Vibration*, Cambridge University Press, Cambridge, UK.

[17] Hurty, W. C., 1965, "Dynamic Analysis of Structural Systems Using Component Modes," AIAA J., **3**, pp. 678–685.

[18] Klosterman, A. L., and Lemon, J. R., 1969, "Building Block Approach to Structural Dynamics," *American Society of Mechanical Engineering Annual Vibration Conference*, publication VIBR-30.

[19] Klosterman, A. L., McClelland, and Sherlock, W. I., 1977, "Dynamic Simulation of Complex Systems Utilizing Experimental and Analytical Techniques," ASME Publication 75-WA/Aero-9.

[20] Ewins, D. J., 1986, "Analysis of Modified or Coupled Structures Using FRF Properties," Internal Report 86002, Dynamics Section, Department of Mechanical Engineering, Imperial College, London, UK.

[21] Craig, Jr., R. R., 1987, "A Review of Time-Domain and Frequency Domain Component-Mode Synthesis Methods," Int. J. Anal. Exp. Modal Anal., **2** pp. 59–72.

[22] Jetmundsen, B., Bielawa, R. L., and Flannelly, W. G., 1988, "Generalized Frequency Domain Substructure Synthesis," J. Am. Helicopter Soc., **33**, pp.

55–64.

[23] Otte, D., Leuridan, J., Grangier, H., and Aquilina, R., 1991, “Prediction of the Dynamics of Structural Assemblies Using Measured FRF Data: Some Improved Data Enhancement Techniques,” *Proc. of the 9th International Modal Analysis Conference (IMAC-1991)*, Florence, Italy, pp. 909–918.

[24] Farhat, C., and Geradin, M., 1992, “A Hybrid Formulation of a Component Mode Synthesis Method,” *33rd Structural Dynamics and Materials Conference*, AIAA paper 92-2383-CP, Dallas, TX, pp. 1783–1796.

[25] Ren, Y., and Beards, C. F., 1993, “A Generalized Receptance Coupling Technique,” *Proc. of the 11th International Modal Analysis Conference (IMAC-1993)*, Kissimmee, FL, pp. 868–871.

[26] Ren, Y., and Beards, C. F., 1995, “On Substructure Synthesis with FRF Data,” J. Sound Vib., **185**, pp. 845–866.

[27] Ewins, D. J., 2000, *Modal Testing: Theory, Practice and Application*, 2nd ed., Research Studies Press, Philadelphia, PA.

[28] Lui, W., and Ewins, D. J., 2002, “Substructure Synthesis Via Elastic Media,” J. Sound Vib., **257**, pp. 361–379.

[29] Ferreira, J. V., and Ewins, D. J., 1996, “Nonlinear Receptance Coupling Approach Based on Describing Functions,” *Proc. of the 14th International Modal Analysis Conference (IMAC-1996)*, Dearborn, MI, pp. 1034–1040.

[30] Yigit, A. S., and Ulsoy, A. G., 2002, “Dynamic Stiffness Evaluation for Reconfigurable Machine Tools Including Weakly Non-Linear Joint Characteristics,” *Proceedings of the I MECH E Part B Journal of Engineering Manufacture*, **216**, pp. 87–101.

[31] Park, S., Altintas, Y., and Movahhedy, M., 2003, “Receptance Coupling for End Mills,” Int. J. Mach. Tools Manuf., **43**, pp. 889–896.

[32] Ferreira, J., and Ewins, D., 1995, “Nonlinear Receptance Coupling Approach Based on Describing Functions,” *Proc. of the 14th International Modal Analysis Conference*, Dearborn, MI, pp. 1034–1040.

[33] Bishop, R., 1955, “The Analysis of Vibrating Systems which Embody Beams in Flexure,” Proc. Inst. Mech. Eng., **169**, pp. 1031–1050.

[34] Weaver, Jr., W., Timoshenko, P., and Young, D., 1990, *Vibration Problems in Engineering*, 5th Ed., John Wiley and Sons, New York.

[35] Sattinger, S., 1980, “A Method for Experimentally Determining Rotational Mobilities of Structures,” Shock Vibr. Bull., **50**, pp. 17–27.

[36] Mathworks, 2002, *Matlab 6.5.0 Release 13: High-Performance Numeric Computation and Visualization Software*, Natick, MA.

[37] Schmitz, T., Ziegert, J., Burns, T., Dutterer, B., and Winfough, W., 2004, “Tool-Length Dependent Stability Surfaces,” Mach. Sci. Technol., **8**(3), pp. 1–21.

[38] Altintas, Y. and Budak, E., 1995, “Analytical Prediction of Stability Lobes in Milling,” CIRP Ann., **44**, pp. 357–362.

[39] Yokoyama, T., 1990, “Vibrations of a Hanging Timoshenko Beam Under Gravity,” J. Sound Vib., **141**, pp. 245–258.

[40] Hutchinson, J., 2001, “Shear Coefficients for Timoshenko Beam Theory,” J. Appl. Mech., **68**, pp. 87–92.